Int J Adv Manuf Technol (2004) 24: 640–646
DOI 10.1007/s00170-003-1747-2

ORIGINAL ARTICLE

Jiwang Yan · Jun'ichi Tamaki · Katsuo Syoji · Tsunemoto Kuriyagawa

Single-point diamond turning of CaF_2 for nanometric surface

Received: 17 September 2002 / Accepted: 10 April 2003 / Published online: 19 May 2004

Abstract Single-crystal CaF_2 is an important optical material. In this work, single-point diamond turning experiments were performed to investigate the nanometric machining characteristics of CaF_2. The effects of tool feed, tool rake angle, workpiece crystal orientation and cutting fluid were examined. It was found that two major types of microfracturing differing in mechanism limited the possibility of ductile regime machining. The critical conditions for microfracturing depend strongly on the tool rake angle and the type of cutting fluid. The results also indicate that one type of the microfractures is caused by thermal effect, and can be completely eliminated by using a sufficiently small undeformed chip thickness and an appropriate negative rake angle under dry cutting conditions. Continuous chips and ductile-cut surfaces with nanometric roughness were generated.

Keywords CaF_2 · Calcium fluoride · Diamond turning · Ductile regime machining · Microfracture · Dry cutting

1 Introduction

Calcium fluoride (CaF_2) is a transparent colourless single crystal with a fluorite-type crystal structure. It has extremely high permeability and a refractive index ranging from 125 nm (ultraviolet) to 12 μm (infrared) wavelength and excellent colour-aberration compensation ability. Therefore, CaF_2 is not only an optical substrate material for dark-field imaging systems but also an indispensable lens substrate material for large-scale semiconductor lithography systems. Especially when 193 and 157 nm lithography systems are developed, where CaF_2 components are utilised to replace fused SiO_2, CaF_2 is becoming the most commercially important material within the optics community. Specific applications for CaF_2 include 193 nm excimer laser components, chromatic aberration correction of 193 nm stepper lens systems, and stepper lenses for future 157 nm systems [1].

The optical performance of CaF_2 is strongly influenced by surface quality. It has been shown that laser damage performance for CaF_2 is strongly dependent on surface preparation [2] and transmission performance for CaF_2 depends significantly on surface roughness [3]. On the other hand, CaF_2 is a typically brittle material, having very low fracture toughness and low hardness. Also, CaF_2 has an extremely high thermal expansion coefficient and a very low thermal conductivity. Some of the properties of CaF_2 are listed in Table 1 [4], where the corresponding properties for single-crystal silicon are also listed for reference. Due to its delicate nature, CaF_2 is very difficult to machine. Conventionally, CaF_2 has to be finished by lapping and subsequent mechanical polishing. However, the polishing processes are too difficult to be automatically controlled to produce complex shape such as aspherical and diffractive optical surfaces, which are required more and more often [5].

An alternative machining method for CaF_2 would be single-point diamond turning (SPDT). SPDT is an ultra-precision metal cutting technology capable of machining high-accuracy components with complex geometries [6]. In the last decade, SPDT has also been extended for precision machining of brittle materials such as glass, silicon, germanium and so on [7–15]. However, little effort is currently placed on the SPDT of CaF_2. In the present work, we conducted SPDT experiments in the micrometer-nanometer scale on CaF_2 in order to examine the possible conditions for fabricating high-quality optical surfaces.

2 Experimental procedures

Most of the available literature on ductile-regime turning of brittle materials is concerned with the use of round-nosed diamond tools [8–12, 14], the machining model for which was given by

J. Yan (✉) · J. Tamaki
Department of Mechanical Engineering,
Kitami Institute of Technology,
Koen-cho 165, Kitami, Hokkaido 090-8507, Japan
E-mail: yanjw@mail.kitami-it.ac.jp
Tel.: +81-157-26-9206
Fax: +81-157-23-9375

K. Syoji · T. Kuriyagawa
Department of Mechatronics and Precision Engineering,
Tohoku University,
Aramaki-Aoba-01, Aoba-ku, Sendai 980-8579, Japan

Table 1. Optical, mechanical and thermal properties of CaF_2 and a comparison with silicon

Property	CaF_2	Silicon
Permeable wavelength (μm)	0.125∼12	1.2∼15
Reflection loss (%)	5.6 (4 μm)	46.1 (10 μm)
Crystal structure	Fluorite	Diamond
Cleavage plane	{111}	{111}
Slip system	$\{001\}\langle 1\bar{1}0\rangle$	$\{111\}\langle 1\bar{1}0\rangle$
Knoop hardness (kg/mm^2)	158.3	1150
Young's modulus (GPa)	75 (25°C)	170
Thermal conductivity index (cal/cmSec°C)	0.0232 (36°C)	0.39 (40°C)
Coefficient of thermal expansion (10^{-6}/°C)	24 (20∼60°C)	4.15 (10∼50°C)
Melting point (°C)	1360	1420
Specific heat (cal/g°C)	0.204 (0°C)	0.168 (25°C)

Blackly et al. [9]. When machining with a round-nosed tool, the machining scale (undeformed chip thickness) is not constant along the cutting edge. Thus, a truly ductile response only occurs along the apex of the tool tip where the undeformed chip thickness is smaller than a critical value (critical chip thickness or critical depth, d_c), while the upper material will be fractured.

Instead of the round-nosed tool, the authors propose a straight-nosed diamond tool for ductile-regime turning [16]. In this case, as schematically shown in Fig. 1, the undeformed chip thickness h is uniform across the entire width of the cutting edge. Undeformed chip thickness h is independent of the depth of cut a, and is determined by tool feed f and cutting edge angle κ, according to the equation

$$h = f \cdot \sin\kappa. \tag{1}$$

Therefore, through the use of a sufficiently small cutting edge angle κ or a sufficiently small tool feed f, this method makes it possible to thin the undeformed chip thickness to the nanometric range over the entire cutting region. This tool geometry provides significant width to undeformed chip thickness ratio to ensure plane strain conditions and hence the relationship between the material removal behaviour and the machining scale is unambiguous and readily studied. In the experiments described below, SPDT tests were carried out using straight-nosed diamond tools.

The experiments were carried out on an ultra-precision lathe with a hydrostatic bearing spindle and two hydrostatic slide tables along the X and Z axes respectively. A specially designed tool post allows the tool to be rotated along the B-axis, which is necessary for the adjustment of the cutting edge angle. Pre-

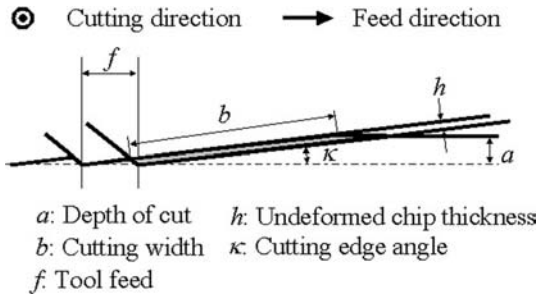

Fig. 1. Schematic of the cutting model of a straight-nosed diamond tool

polished single-crystal CaF_2 wafers with (111) orientation and dimensions of 50 mm diameter and 5 mm thickness were used as specimens. Figure 2 shows the crystal orientations of various cutting directions as the workpiece rotates. The specimens were bonded on diamond-turned aluminium blanks using a 50 °C heat-softened glue and then vacuum-chucked to the machine spindle.

The rake angle of the diamond tool was varied from 0 to −60° while keeping the relief angle constant at 6°. Before cutting, the tools were examined with a special scanning electron microscope (SEM) that has two electron detectors (secondary electron detector and reflecting electron detector) and enables three-dimensional analysing. The average cutting edge radius of the diamond tools was estimated to be 20 ∼ 40 nm.

Undeformed chip thickness was varied from a few nanometers to approximately 1 μm by varying the tool feed from 1 to 40 μm and the cutting edge angle in the range of 0.5 to 1.5°. The depth of cut was varied in the range of 1 ∼ 5 μm. The spindle rotation rate was constant at 1500 rpm. Face turning was performed at the diameter range from 10 to 50 mm with a corresponding cutting speed of 47 ∼ 235.5 m/min. Kerosene mist, kerosene liquid, water, dehydrated methanol and acetone were used as cutting fluids.

The machined surfaces were observed using an SEM and measured using a stylus-profiling instrument, Form TalySurf,

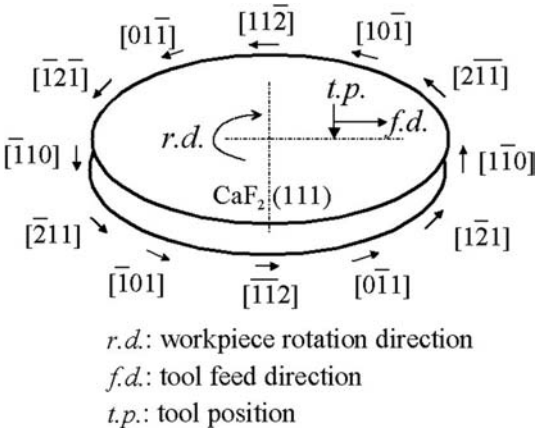

Fig. 2. Presentation of the crystal orientations corresponding to various cutting directions in the SPDT of Caf_2 (111)

and an atomic force microscope (AFM). Chips removed from the specimen were observed with the SEM.

3 Results and discussion

3.1 Microfracturing

At first, a cutting test was performed by continuously varying the tool feed f in the range of $1 \sim 40$ μm at a constant cutting edge angle ($\kappa = 1.5°$), a constant depth of cut ($a = 5$ μm) with a $-30°$ rake angle tool and kerosene mist as coolant. Under these conditions the undeformed chip thickness varies from to 26 nm to 1 μm. The cut was made at the diameter of 30 mm on the workpiece, corresponding to a cutting speed of 141 m/min. Figure 3 is an SEM photograph of the surface of $[\overline{1}\overline{1}2]$ orientation machined under these conditions. From left to right in the figure, the tool feed was decreased from 40 μm to 1 μm and then increased to 40 μm again. The surface can be divided into two kinds of regions: high feed regions on the left and right (region A), and low feed region in the middle (region B). It can be seen that in region A, microfractures of the order of 1 to 10 μm occurred densely, and in region B, fractures as large as a few hundred micrometers occurred. Here we term the two types of microfractures type A and type B, respectively. High magnification observations showed that the average value of the critical tool feed at which A-type microfracturing began to occur (f_{c1}) was 5.5 μm, and the critical tool feed for B-type microfracturing (f_{c2}) was 3.5 μm. These two types of microfracturing limit the ductile machining regime to be within the tool feed range of $3.5 \sim 5.5$ μm.

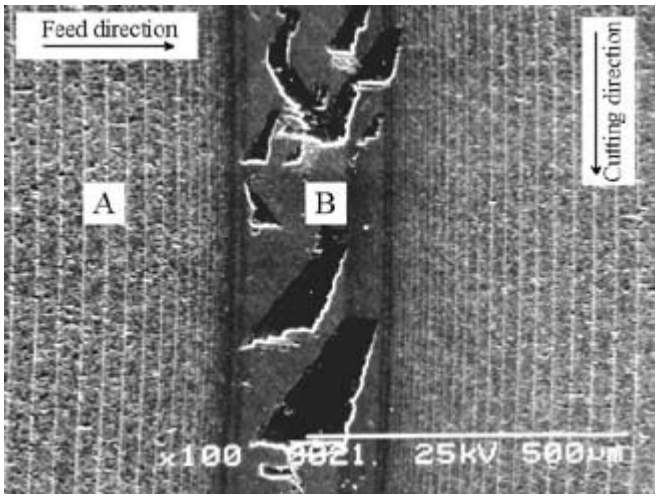

Fig. 3. SEM photograph of the CaF_2 surface machined at continuously varied tool feed using kerosene as coolant. Regions A and B correspond to high tool feed region and low tool feed region, respectively, with differing micro fracture regimes

The A-type microfracturing under high feed conditions has also been reported in the SPDT of most brittle materials such as silicon [14, 16] and germanium [8, 9], but the B-type microfracturing under low feed conditions can not be found in available literature. In order to examine the differences in microfracturing mechanism, high-magnification SEM observations of the microfractures were performed. Figure 4a is an SEM photograph of the surface of region A in Fig. 3, where the tool feed was 35 μm (undeformed chip thickness 935 nm). The surface is densely covered with microcraters. The profiles of the craters are irregular and twisted, exhibiting a plastic flow appearance. Figure 4b shows a typical cross-sectional profile of a microcrater, measured along the cutting direction. The profile is in the form of the V-shape and the maximum depth of the crater is $1 \sim 2$ μm.

Figure 5a is an SEM photograph of the surface of region B in Fig. 3, where the tool feed was 1 μm (undeformed chip thickness 26 nm). Despite that the undeformed chip thickness is small, microfractures occurred at a larger scale than those in Fig. 4. These microfractures have straight fringes with smooth and flat fractured surfaces. Figure 5b shows a typical cross-sectional profile of the fracture. The fracture has a U-shape in cross section, with a flat bottom approximately parallel to the machined surface. The maximum depth of the fracture is approximately 6 μm, more than 3 times that in Fig. 4b.

3.2 Effect of crystal orientation

The observations of microfractures were also performed on other orientations of the specimen. The results show that the A-type microfracturing is strongly affected by the crystal orientations. Along $[2\overline{1}\overline{1}]$ and $[\overline{1}2\overline{1}]$, the finished surface appears to be the same as that produced along $[\overline{1}\overline{1}2]$, as described in Fig. 4. However, along any one of the $\langle 11\overline{2}\rangle$ orientations, the appearance

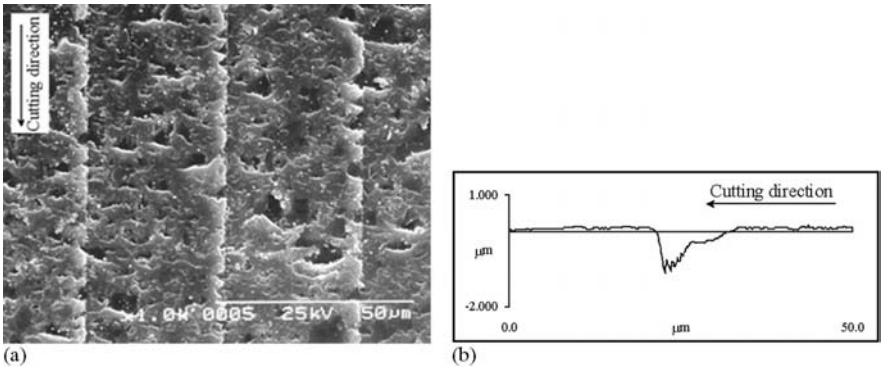

Fig. 4a,b. The A-type micro fractures formed when cutting parallel to $[\overline{1}\overline{1}2]$: **a** SEM photograph of the A-region surface, **b** Cross-sectional profile of a micro crater

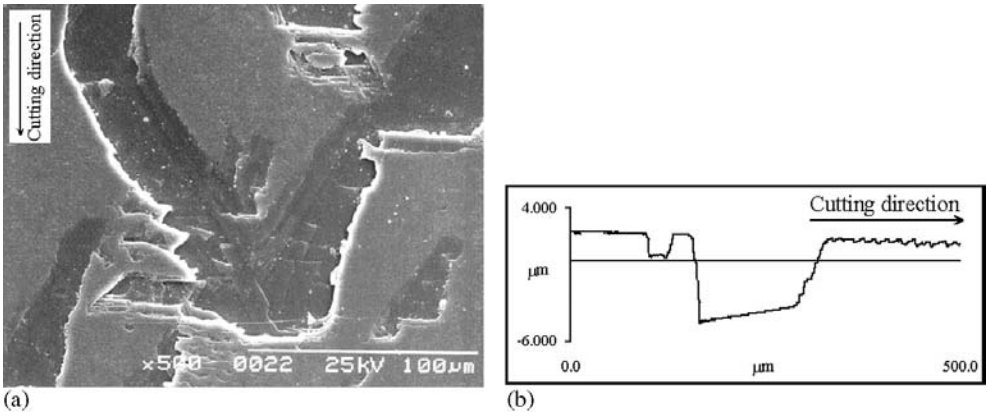

Fig. 5a,b. The B-type micro fracture formed when cutting parallel to $[\bar{1}12]$: **a** High-magnification SEM photograph of the B-region surface, **b** Cross-sectional profile of a micro fracture

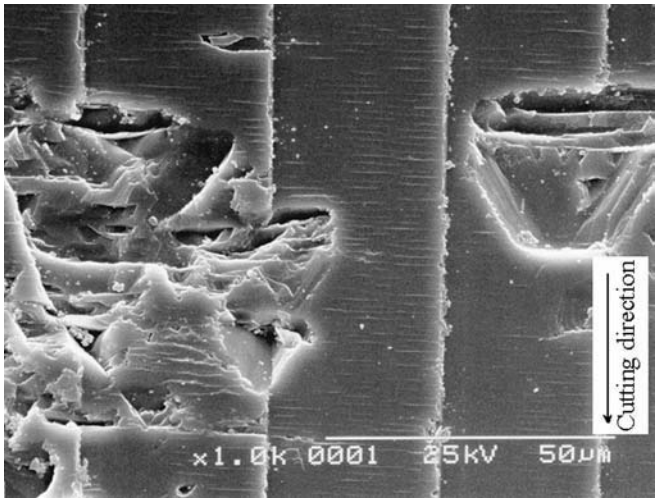

Fig. 6. SEM photograph of the machined surface cut parallel to $[11\bar{2}]$: showing triangular micro fractures

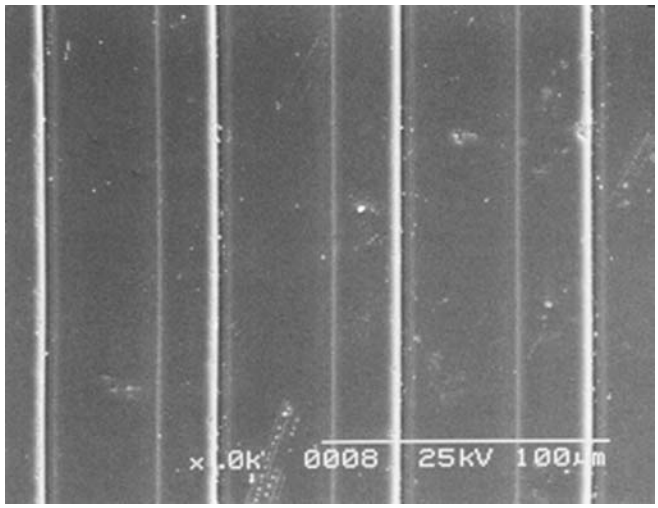

Fig. 7. SEM photograph of the machined surface cut parallel to $[\bar{1}01]$

of the microfractures was significantly different from those produced in the $\langle\bar{1}12\rangle$ orientations. As shown in Fig. 6, despite that some areas of the machined surface are smooth, craters of a few microns in width are observed. These craters have triangular profiles. The depth of the craters was greater than 10 μm, far larger than those in Fig. 4b. In contrast to these orientations, when the cutting direction was parallel to any one of the $\langle\bar{1}01\rangle$ orientations, the machined surfaces tend to be ductile cut, and no microfractures were produced, as shown in Fig. 7.

The above results indicate that the A-type microfracture is due to both the size effect and the crystallographic effect of ductile-brittle transition. At high tool feed conditions, the machining scale (undeformed chip thickness) is large thus it becomes energetically favourable to produce brittle fracture. On the other hand, the machining mechanism will also depend on the relationship between the crystal orientation and cutting forces. A cutting force produces tensile/shear stress along the cleavage/slip systems, respectively, and it is the behaviour of the cleavage/slip systems that determines whether fracture or plastic deformation occurs. The cleavage plane of single-crystal CaF_2 is {111} and the preferred slip system is $\{001\}\langle1\bar{1}0\rangle$ [17]. Thus when cutting along $[11\bar{2}]$, the cleavage plane $(11\bar{1})$ will be activated immediately, resulting in cleavage fractures (see Fig. 6). When cutting along $[\bar{1}12]$, two slip systems, $(010)[10\bar{1}]$ and $(100)[0\bar{1}1]$, become symmetrical to the cutting condition thus slip will be restricted due to interaction between slip systems [12]. The material removal under such conditions involves a mixture of brittle mode and ductile mode, resulting in surface texture as shown in Fig. 4. However, when cutting along $[10\bar{1}]$, the shear stress acting along the slip system $(010)[10\bar{1}]$ becomes dominant. According to the Schmid's law [17], the above slip systems will be activated and slip deformation will occur, leading to a ductile-regime cut surface (see Fig. 7).

Compared to A-type microfracturing, B-type microfractures were less dependent on crystal orientation. Along all orientations, B-type microfractures occurred with the same severity and appearances. The bottom surfaces of the microfractures were flat and approximately parallel to the machined surface. The depths of the fractures were also similar. These results indicate that a B-type microfracture is initiated along the (111) crystal planes parallel to the machined surface and is independent of the cutting direction.

3.3 Effect of tool rake angle

In the SPDT of brittle materials such as silicon and germanium, it has been known that a negative rake angle is essential for ductile material removal [8–10, 14, 15, 18]. We also found that at extremely high negative rake angles ($-70 \sim -80°$), the critical chip thickness (or critical depth, d_c) begins to decrease due to difficulties in chip flow and the formation of severe subsurface damage [19]. The optimum tool rake angle for cutting silicon has been demonstrated to be approximately $-40°$ [19]. In the present experiments, the tool rake angle was varied in the range of $0 \sim -60°$ to examine the rake angle effect. Other conditions are the same as Sect. 3.1.

Figure 8 shows the variation in the critical tool feeds f_{c1} and f_{c2} with respect to the tool rake angle. The measurement of f_{c1} and f_{c2} was made at the $[\overline{1}12]$ orientation, with error bars showing the maximum and minimum values. In the figure, only the region below the curve of f_{c1} and above the curve of f_{c2} ($f_{c1} > f > f_{c2}$) is a ductile region, while other regions, shaded in the figure, are brittle regions. It can be seen that as tool rake angle changes from 0 to $-60°$, both f_{c1} and f_{c2} increases. However, the increase in f_{c2} is greater than the increase in f_{c1}, such that the resulting ductile region becomes narrower as the tool rake angle decreases. The $-20°$ tool rake angle corresponds to the widest ductile region. When the rake angle decreased to $-60°$, f_{c2} becomes larger than f_{c1}, thus no ductile region exists. Figure 9 is an SEM photograph of a surface machined using a tool with a $-60°$ rake angle. The entire surface is severely damaged with connecting B-type microfractures. These results are significantly different from the results for diamond turning of silicon [19].

3.4 Effect of cutting fluid

Kerosene liquid, water, dehydrated methanol and acetone were investigated as cutting fluids, in addition to kerosene mist, in order to investigate the effect of the cutting fluid on material removal. These cutting fluids are known to have significant ability to improve tool life in SPDT. Figure 10 shows the variation in the critical tool feeds f_{c1} and f_{c2} when different cutting fluids were used at the $-30°$ rake angle. It can be seen that cutting fluids that increase f_{c2} have the opposite effect on f_{c1}, and vice versa. Among the five kinds of cutting fluids, kerosene mist (1) produces the widest ductile region, whereas only brittle cutting can be achieved using acetone or methanol (4 and 5).

Generally, the effect of a cutting fluid involves thermal, tribological and chemical aspects. While the origin of B-type microfracturing can not be clarified on the basis of the present results, one possible reason may be attributable to thermal effects. As known from cutting principles, the heat generated by cutting deformation causes the temperature of the near surface region to rise significantly compared to the interior material. In diamond turning of metals such as copper and aluminium, the surface temperature rise has been reported to be 200 °C and 220 °C, respec-

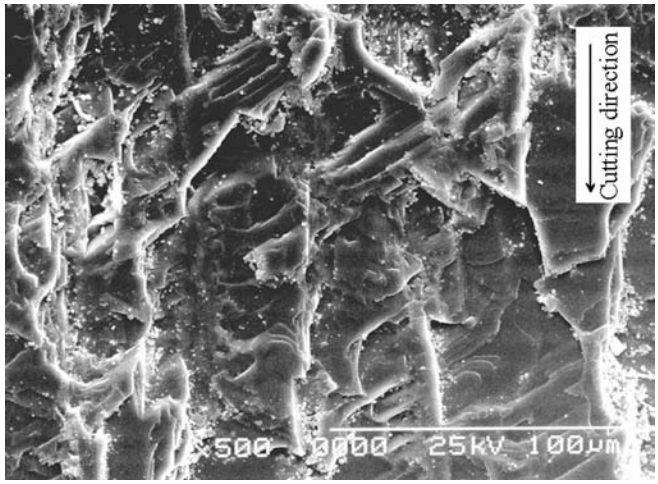

Fig. 9. SEM photograph of the surface machined using a diamond tool with a $-60°$ rake angle during wet cutting

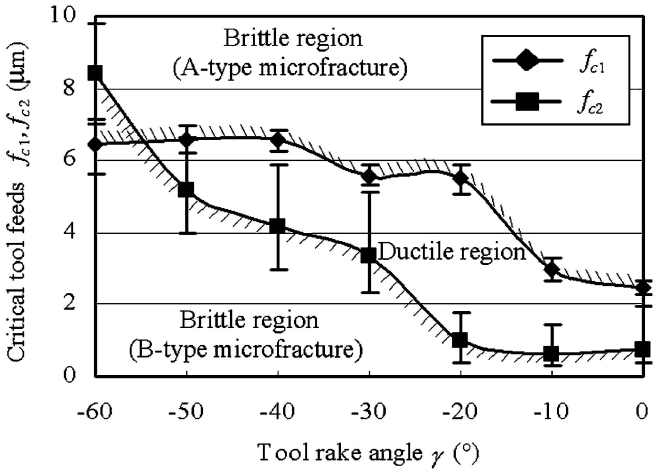

Fig. 8. Effect of tool rake angle on the critical tool feeds for the two microfracturing regimes

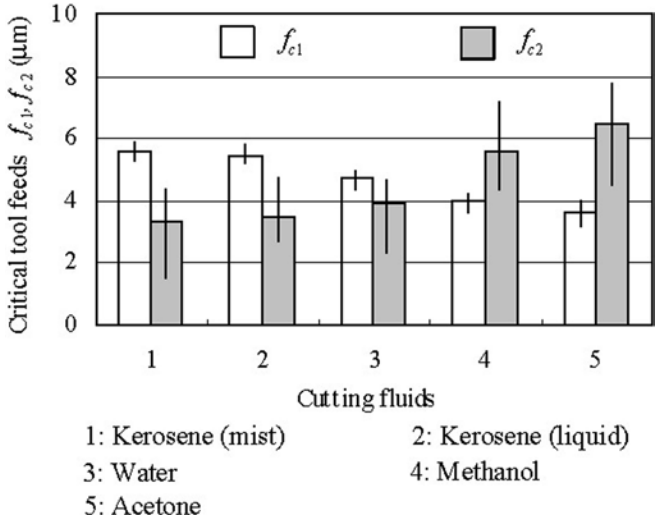

Fig. 10. Effects of cutting fluids on the critical tool feeds for the two types of micro fractures when cutting with a $-30°$ rake angle tool

tively [20, 21]. A similar temperature rise may take place in the SPDT of brittle material if the material is removed in a ductile mode. The high surface temperature, however, will drop rapidly due to the cooling effect when a cutting fluid is used. The cyclic temperature fluctuation will cause tensile stress in the near surface layer, eventually leading to crack initiation along the cleavage planes of the crystal. The fact that the B-type microfracturing is significant for CaF_2 but insignificant for silicon and metals would be due to the fact that the thermal conductivity of CaF_2 is extremely low (0.06 times that of silicon) and thermal expansion coefficient is extremely high (5.8 times that of silicon). This thermal property leads to a significant temperature gradient and consequently a sharp stress gradient between the near surface layer and the internal region, which drives crack initiation. The above explanation is in good agreement with the experimental results of tool feed effect and rake angle effect. Under an extremely low tool feed, both the specific cutting energy per tool pass and the number of tool pass per unit surface area increases significantly, which results in a high temperature rise. Similarly, a higher negative rake angle also leads to a higher temperature rise, increasing the possibility of B-type microfracturing.

If the above conjecture is true, it may be possible to eliminate B-type microfracturing by avoiding the use of cutting fluids. Because in dry cutting there is no rapid cooling effect, the cutting heat in the surface layer can be conducted gradually into the internal region and the environment, preventing the formation of sharp temperature gradient. Based on this assumption, the authors performed SPDT tests under dry conditions. Figure 11 is an SEM photograph of the surface machined at varied tool feed under dry conditions, where all other conditions are the same as in Fig. 3. In the high feed region (A), similar to Fig. 3, A-type microfracturing occurs. However, in the low feed region (B), smooth ductile surfaces were obtained without any visible damage. Also, it is noticed that the critical tool feed for A-type microfracturing f_{c1} (7 μm) has been greater than that of cutting using a fluid.

Finally a small CaF_2 specimen, 25 mm in diameter and 3 mm in thickness, was machined under dry conditions for the purpose of examining the surface by AFM. A $-20°$ rake angle tool was used at the tool feed of 1 μm, depth of cut of 1 μm and cutting edge angle of 0.6°. Under these conditions, the whole surface of the specimen was ductile cut. Figure 12 is an AFM image of the surface. The surface consists of periodical tool feed marks with a surface roughness of 15 nm R_y and 2.4 nm Ra. Figure 13 is an SEM photograph of the chips collected under the above conditions. The chips are formed as continuous ribbons, similar to those produced by metal cutting. These chips indicate that the workmaterial has been removed in a completely ductile mode.

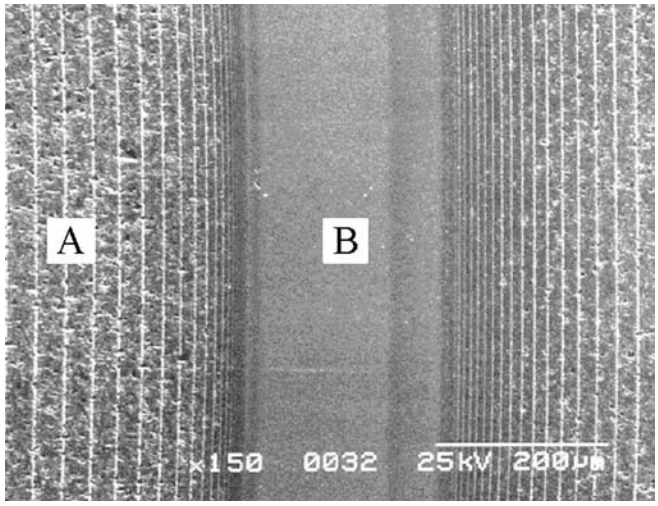

Fig. 11. SEM photograph of the CaF_2 surface machined at continuously varied tool feed under dry cutting conditions, showing micro fractures in the high-feed region (A) but no micro fractures in the low-feed region (B)

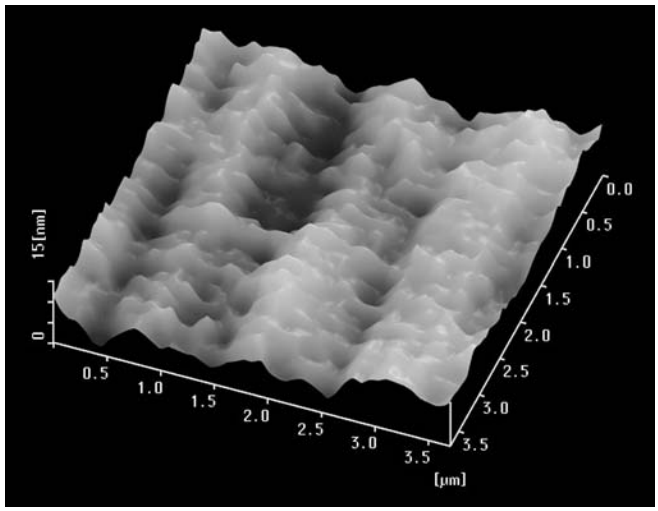

Fig. 12. AFM image of the CaF_2 surface machined at a tool feed of 1 μm under dry cutting conditions. The surface is completely ductile cut and the surface roughness is 15 nm Ry and 2.4 nm Ra

4 Conclusions

Single-crystal CaF_2 has been machined in the micrometer-nanometer level by single-point diamond turning under various conditions. The experimental results can be summarised as follows:

1. Two major types of microfractures occur during wet cutting, namely, Type A and Type B. The A-type microfracture is one to 10 microns in size and occurs under high tool feed conditions, whereas the B-type microfracture is on the order of 100 microns in size and occurs under extremely low tool feed conditions. The A-type microfracture is due to the size effect and the crystallographic effect of the ductile-brittle transition, while the B-type microfracture results probably from the thermal effect. As a result, ductile regime machining is only possible when the tool feed is between the two critical tool feeds of these two types of microfracturing.
2. A-type microfracturing is significantly affected by the workpiece crystal orientation. The $\langle 11\bar{2}\rangle$ orientations correspond to the largest fracture depth while the $\langle \bar{1}01\rangle$ orientations are

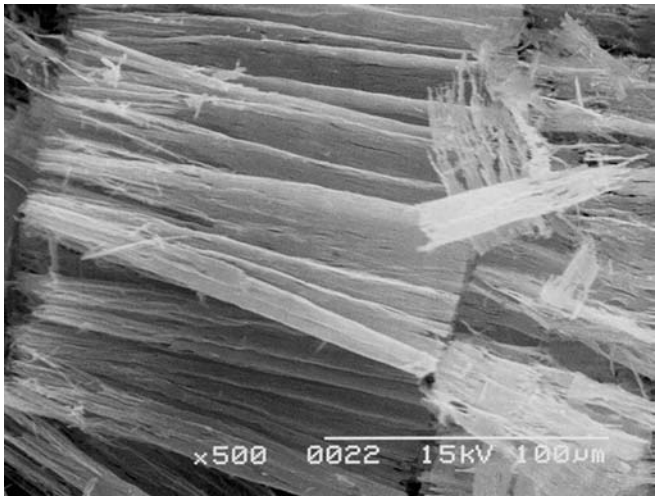

Fig. 13. SEM photograph of continuous CaF_2 chips obtained in dry cutting, indicating ductile-regime material removal

most easily to be ductile cut. B-type microfracturing is independent on the crystal orientation.

3. The critical tool feeds of both types of microfracturing are significantly affected by tool rake angle. The −20° rake angle corresponds to the broadest tool feed range for ductile regime machining.
4. B-type microfracturing depends on the cutting fluid type. Performing dry cutting can eliminate B-type microfracturing. During dry cutting, the formation of continuous chips and ductile-cut surfaces with nanometric roughness were confirmed.

The future direction of this work is along two lines, namely: investigating the thermal and crystallographic effect on the machining mechanism in detail and applying dry cutting to the fabrication of aspheric and diffraction optical elements of CaF_2.

Acknowledgement This work was funded by the Japan New Energy and Industrial Technology Development Organization (Project No. 01A38004) and partly supported by the Industrial/Academic Cooperative Research Committee on Ultra-Precision Ultra-High Speed Machining, Japan Society for Precision Engineering (JSPE). The authors would like to thank the Tokyo Diamond Tool Co. for providing the diamond tools, and OKEN Co. Ltd. for providing the specimens and property data for this study. The first author (J. Yan) also expresses his gratitude to Prof. Y. Namba of Chubu University, Mr. M. Negishi of the Core Technology Centre, Nikon Corporation and Mr. H. Ito of the Production Engineering Department, Olympus Optical Co. Ltd., for providing useful information.

References

1. Liberman V, Bloomstein TM, Rothschild M, Sedlacek JHC, Uttaro RS, Bates AK, Peski CV, Orvek K (1999) Materials issues for optical components and photomasks in 157 nm lithography. J Vac Sci Technol B 17:3273–3279
2. Stenzel E, Gogoll S, Sils J, Huisinga M, Johansen H, Kastner G, Reichling M, Matthias E (1997) Laser damage of alkaline-earth fluorides at 248 nm and the influence of polishing grades. Appl Surf Sci 109–110:162–167
3. Retherford RS, Sabia R, Sokira VP (2001) Effect of surface quality on transmission performance for (111) CaF_2. Appl Surf Sci 183(3–4):264–269
4. Technical Document of OKEN Co. Ltd. (2000)
5. O'Shea DC (1985) Element of modern optical design. Wiley, New York
6. Ikawa N, Donaldson RR, Komanduri R, Konig W, McKeown PA, Moriwaki T, Stowers IF (1991) Ultra-precision metal cutting – The past, the present and the future. Ann CIRP 40(2):587–594
7. Puttick KE, Rudman MR, Smith KJ, Franks A, Lindsey K (1989) Single point diamond machining of glass. Proc Roy Soc A 426:19–30
8. Blake PN, Scattergood RO (1990) Ductile regime machining of germanium and silicon. J Amer Ceram Soc 73(4):949–957
9. Blackly WS, Scattergood RO (1991) Ductile-regime machining model for diamond turning of brittle materials. Prec Eng 13(2):95–103
10. Nakasuji T, Kodera S, Hara S, Matsunaga H, Ikawa N, Shimada S (1990) Diamond turning of brittle materials for optical components. Ann CIRP 39(1):89–92
11. Shore P (1995) Assessment of the precision and cost effectiveness of direct machining "hybrid" type optical surface for IR applications. Proc SPIE 2576:426–431
12. Shibata T, Fujii S, Makino E, Ikeda M (1996) Ductile-regime turning mechanism of single-crystal silicon. Prec Eng 18(2/3):130–137
13. Kunz RR, Clark HR, Nitishin PM, Rothschild M, Ahern BS (1996) High resolution studies of crystalline damage induced by lapping and single-point diamond machining of Si (100). J Mater Res 11(5):1228–1237
14. Leung TP, Lee WB, Lu XM (1998) Diamond turning of silicon substrates in ductile-regime. J Mater Proc Technol 73:42–48
15. Yan J, Yoshino M, Kuriyagawa T, Shirakashi T, Syoji K, Komanduri R (2001) On the ductile machining of silicon for micro electro-mechanical systems (MEMS), opto-electronic and optical applications. Mater Sci Eng A 297(1–2):230–234
16. Yan J, Syoji K, Kuriyagawa T, Suzuki H (2002) Ductile regime turning at large feed rates. J Mater Process Technol 121:363–372
17. Hertzberg RW (1983) Deformation and fracture mechanics of engineering materials. Wiley, New York
18. Lucca DA, Chou P, Hocken RJ (1998) Effect of tool edge geometry on the nanometric cutting of Ge. Ann CIRP 47(1):475–478
19. Yan J, Syoji K, Kuriyagawa T (2000) Ductile-brittle transition under large negative rake angles. J Japan Soc Prec Eng 66(7):1130–1134, in Japanese
20. Iwata K, Moriwaki T, Okuda K (1987) Analysis of cutting temperature in ultra-high precision diamond cutting of copper. J Japan Soc Prec Eng 53(8):1253–1258, in Japanese
21. Ueda T, Sato M, Nakayama K (1998) The temperature of a single crystal diamond tool in turning. Ann CIRP 47(1):41–44